

# Large-Scale Orientation Dependent Heating from a Single Irradiated Gold Nanorod

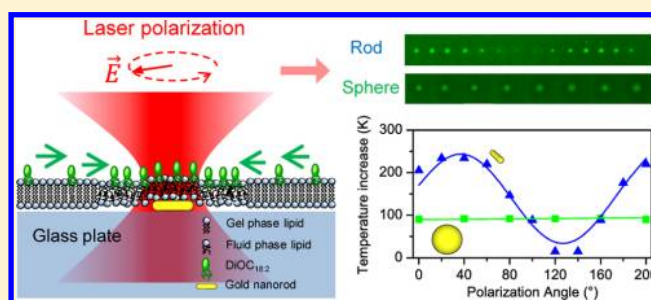
Haiyan Ma, Poul M. Bendix, and Lene B. Oddershede\*

Niels Bohr Institute, University of Copenhagen, Denmark

**S** Supporting Information

**ABSTRACT:** We quantify the extreme heating associated with resonant irradiation of individual gold nanorods by using a novel assay based on partitioning of lipophilic dyes between membrane phases. The temperature increase is sensitively dependent on the angle between the laser polarization and the orientation of the nanorod. A dramatic and irreversible decrease in the heating of a nanorod occurs at high-illumination intensities; this effect is attributed to surface melting of the nanorod causing it to restructure into a more spherical shape and lose its extreme photothermal properties.

**KEYWORDS:** Gold nanorod, photothermal effect, lipid bilayer, molecular partitioning, surface plasmon resonance, polarization



The use of plasmonic coupling between metallic nanostructures and near-infrared (NIR) light is emerging as a powerful tool to locally heat biological material. Since biological material is relatively transparent to NIR light, it is of great interest in the context of localized photothermal therapy<sup>1,2</sup> *in vivo* visualization<sup>3–5</sup> or drug delivery<sup>6</sup> to design small nanostructures with peak absorption of NIR light. If irradiated at its surface plasmon resonance frequency, a metallic nanoparticle efficiently converts the absorbed energy into heat that is locally dissipated, thus resulting in a significant temperature increase around the nanoparticle. The surface plasmon resonance frequency of gold nanorods has been shown to depend sensitively on their aspect ratio and can therefore be tuned to the biologically transparent NIR window by increasing their aspect ratio.<sup>7–9</sup>

The inherent asymmetry of a nanorod results in two resonant wavelengths, the longitudinal and the transverse, depending on whether the polarization is parallel to or perpendicular to the long axis of the rod. This high degree of polarization anisotropy can be utilized for orientation sensing.<sup>10</sup> Metallic nanoparticles can be optically trapped in three dimensions<sup>11,12</sup> and gold nanorods as thin as 8 nm have been found to align along the polarization of the trapping laser<sup>13</sup> while optically trapped in three dimensions. The torque exerted by the optical trap on a trapped gold nanorod has been found by monitoring the Brownian fluctuations in the trap, which also yielded an estimate of the associated heating.<sup>14</sup> However, since the nanorod aligns with the polarization of the trapping laser, it is not possible to measure the anisotropy of nanorod absorption at different angles using this method. Moreover, since the trapping potential is relatively weak, there will be considerable axial, lateral, and rotational fluctuations of the heated rod in the laser focus which will smear out any

orientation dependence and displace the rod from the most intense region of the laser beam.

The energy absorbed by an irradiated nanorod is dissipated as heat that could cause it to melt and restructure into a spherical shape as favored by surface tension. The structural stability of nanorods exposed to high temperatures has been measured by irradiating rods with pulsed lasers<sup>15</sup> or simply by incubating nanorods at various temperatures.<sup>16</sup> A gradual conversion of gold nanorods into spheres was found to start already at 200–300 °C, which is well below the bulk melting temperature of gold. Accordingly, it was recently shown that the photothermal effect in cells conjugated with high density of gold nanorods could be radically changed by laser irradiation probably because the gold nanorods underwent thermally induced shape changes.<sup>17</sup>

A few methods have been developed to measure the temperature of irradiated metallic nanoparticles.<sup>18–24</sup> For instance, the well characterized gel-to-fluid phase transition of lipid bilayers has been used to sense the heat dissipated from gold nanospheres irradiated off-resonance by NIR light.<sup>18–20</sup> The interaction between NIR light and metallic nanoparticles is particularly interesting with respect to photothermal applications because biological material is relatively transparent in the NIR spectral range. Another method for local temperature determination around irradiated gold nanostructures utilizes a temperature-dependent photoluminescent thin film of Al<sub>0.94</sub>Ga<sub>0.06</sub>N embedded with Er<sup>3+</sup> ions.<sup>21</sup> Also, thermally induced changes in refractive index or viscosity of the surrounding medium near the heated gold nanoparticles have been used to deduce particle temperatures.<sup>22,24</sup> The temper-

Received: March 21, 2012

Revised: June 22, 2012

Published: June 27, 2012

ature from a large number of nanorods or a single microwire was measured by quantifying the thermally induced change in fluorescence polarization anisotropy.<sup>23</sup> Many of the previously published methods for temperature quantification suffer from a relatively low spatial resolution because light is picked up from a large volume. The dimensions of the focal volume are set by the optical diffraction limit, and if a confocal setting is not used, out of focus light will also be picked up and contribute to the total signal. The temperature gradient around a heated metallic nanoparticle is very steep and can change drastically over a distance comparable to the diameter of the particle. Finally, the interpretation of measurements based on changes in viscosity or fluorescence polarization anisotropy are complicated by the fact that both quantities become nonlinear and less sensitive to temperature changes at temperatures exceeding 100 °C.

Here, we present measurements of the heating of an irradiated single gold nanorod (20 nm × 100 nm) using a continuous wave NIR laser (1064 nm). Our assay is based on the well characterized phase transition of lipid bilayers containing only a single lipid species and on the differential partitioning of fluorescent lipophilic molecules between the two membrane phases. One strength of the method is that it requires no further knowledge about any physical parameters regarding neither the particle, its environment, nor the intensity distribution at the nanoscale. Another strength is its precision; the temperature quantification relies on accurate determination of the phase boundary of a fluorescently marked 2D bilayer (thickness ~5 nm). As no light from below or above the bilayer enters the focal volume, the distance from the nanoparticle to the phase boundary can be accurately determined. Finally, it overcomes the restrictions of other methods where high temperatures are hard to access. Our results show that the temperature rise around a single irradiated gold nanorod is extremely dependent on its orientation with respect to the polarization vector of the heating laser. When the orientation is parallel to the polarization vector, the absorbance and associated surface temperature are significantly higher than that of a gold nanosphere which is 2 orders of magnitude larger in volume and irradiated off-resonance by the NIR laser. Our experimental results are supported by theoretical simulations of the expected absorbance of gold nanorods and spheres using the discrete dipole approximation (DDA).<sup>25</sup> The extreme heating of a nanorod aligned with the polarization vector of the electromagnetic field leads to a partial melting of the rods, thus causing the nanoparticle to develop into a more spherical shape absorbing significantly less in the NIR region; this effect shuts down the extreme heating properties and is important to consider for photothermal applications.

To prepare the samples, gold nanorods were immobilized on a glass surface that was subsequently coated by a gel phase glass supported lipid bilayer. A sketch of the assay is shown in the zoom-in of Figure 1. From TEM images (shown in Supporting Information Figure S1A), we measured the size of the nanorods to be (20.6 ± 2.0) nm × (97.2 ± 25.5) nm (mean ± standard deviation,  $n = 45$ ). The lipid bilayer consisted of DC<sub>15</sub>PC molecules mixed with 2 mol % DiOC<sub>18:2</sub> fluorophores. The experiment was conducted on a Leica SP5 confocal microscope into which a tightly focused 1064 nm laser (Spectra Physics J201-BL-106C) was implemented. Details of the equipment are described in ref 26. The lasers were focused using a Leica oil immersion objective (PL APO, NA = 1.4, ×100). The polarization direction of the laser was controlled by rotating a  $\lambda$ -half wave plate placed in front of the laser, see Figure 1. As

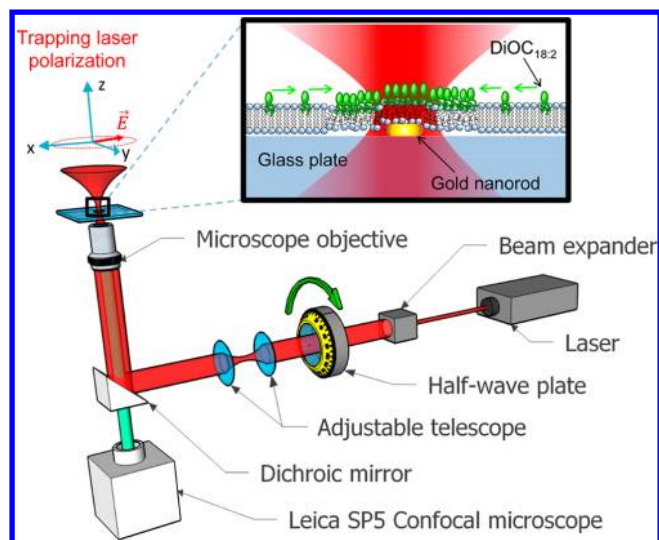


**Figure 1.** Illustration of the experimental setup. The zoom-in shows the sample chamber where a nanorod is immobilized on a glass surface and is covered by a gel phase lipid bilayer DC<sub>15</sub>PC containing a low molar fraction of DiOC<sub>18:2</sub> fluorophores. The fluorophores are excited at 488 nm (in blue) with a Leica SP5 confocal system and the emitted light is collected using a photomultiplier tube. A 1064 nm laser (in pink) is tightly focused by the microscope objective, while the orientation of its polarization (pink arrow in coordinate system) is controlled by a half-wave plate. When the temperature around the irradiated nanorod exceeds the phase transition temperature,  $T_m$ , the lipid bilayer becomes fluid in the vicinity of the irradiated nanorod, and the melted region is visualized by DiOC<sub>18:2</sub> fluorophores which preferentially partition into the fluid phase.

the nanorod was immobilized, the angle between the long axis of the nanorod and the polarization vector of the focused NIR laser (pink arrow in coordinate system in Figure 1) could be controlled. The fluorophores were excited with a 488 nm Argon laser and their emission was collected by a photomultiplier tube in the spectral range  $\lambda = 500\text{--}530$  nm. We also recorded the reflected light from the nanorod at 594 nm using an acousto-optical beam splitter in reflection mode.

The accuracy of the temperature measurements relies on the sharpness of the lipid phase transition as well as on the differential affinity of the lipid fluorophore for the two lipid phases. The phase transition of multilamellar lipid vesicles consisting of DC<sub>15</sub>PC is cooperative with a phase transition temperature at  $T_m \sim 33$  °C and a full width half-maximum (FWHM) of  $\sim 0.1$  °C, (data shown in Supporting Information Figure S2). Our assay was based on a single lipid bilayer and not a multilamellar system that often exhibits cooperative thermodynamic effects. Therefore, we measured the heat capacity of unilamellar vesicles extruded through 100 nm polycarbonate filters. Extrusion through smaller pores would induce broadening of the phase transition due to membrane curvature effects, an artifact not present in our flat supported lipid bilayer. The resulting heat capacity curve of unilamellar DC<sub>15</sub>PC vesicles is shown in Supporting Information Figure S3 (red graph), it has  $T_m \sim 34$  °C and a fwhm of  $\sim 1$  °C. To assess the effect of the fluorescent lipid conjugate, we also measured the differential heat capacity with the fluorophore in the bilayer (Supporting Information Figure S3, yellow graph). The fluorescent conjugate has two unsaturated bonds and consequently lowers the phase transition slightly to  $T_m \sim 33$  °C (FWHM  $\sim 1$  °C). Because of their unsaturated alkyl tails, it

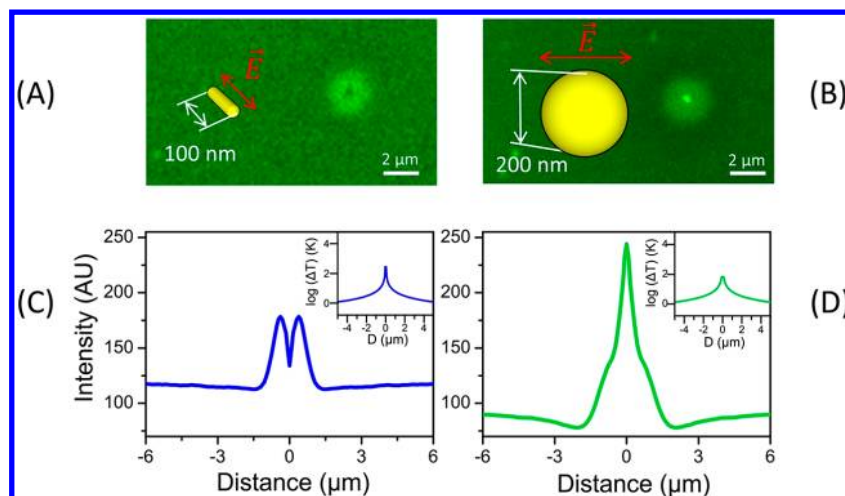


**Figure 2.** Quantification of melting fingerprint and temperature profile. (A,B) Confocal images of fluorophores partitioning in fluid regions around an irradiated gold nanorod (of nominal size 20 nm × 100 nm) (A) or a gold nanosphere (nominal diameter = 200 nm) (B) under identical illumination conditions ( $1.8 \times 10^{10}$  W/m<sup>2</sup>). (C,D) Intensities of fluorophores as a function of distance from the center of the irradiated nanoparticles, (C) is for the rod shown in (A), (D) is for the sphere shown in (B). Insets show the logarithm of the temperature increase as function of distance from the center of the irradiated nanoparticles.

is energetically favorable for DiOC<sub>18:2</sub> fluorophores to partition into the fluid phase of the bilayer.<sup>27</sup> It was crucial to clean the glass coverslips with detergent and organic solvents in sonication bath followed by plasma cleaning (ensuring a highly hydrophilic glass surface) before the bilayer was rapidly added. This preparation caused a ~ 2 nm lubricating layer of water to be present between the glass and the lower leaflet of the bilayer.<sup>28</sup> The phase transition of a glass supported lipid bilayer prepared in this manner has been shown to behave very similar to that of a free bilayer (exhibiting only one main transition).<sup>29</sup> The experiments were performed at an ambient temperature of 27 °C, hence, before switching on the NIR laser, the bilayer was in an ordered gel state. When a nanorod covered by a lipid bilayer was irradiated, it absorbed light and dissipated heat, thus heating up a localized region around the particle. As the temperature exceeded  $T_m$ , the bilayer locally transformed from gel phase to fluid phase, hence, the fluorophores preferably partitioned into the melted region around the nanorod which thus became visible. Figure 2A,B shows typical confocal images of fluorescent bilayers containing an irradiated gold nanorod (A) and nanosphere (B), respectively. The nominal size of the particles (rod, 20 nm × 100 nm; sphere, radius = 100 nm) was below the optical lateral diffraction limit (~150–200 nm for a point scanning confocal microscope), however the fluorescently marked melted region had a circular appearance and a linear size up to a few micrometers, which could be relatively accurately determined. This region was denoted the “fingerprint” of the heating. Our assay was somewhat similar to the assay used in ref 18 with the exceptions that the polarization vector was varied in the present assay and that the fluorophores used preferred to partition into the fluid state, thus yielding a bright fingerprint. The advantage of using a bright fingerprint instead of a dark fingerprint is that the latter could also be caused, for example, by ablation of the lipid bilayer or the bleaching of dyes caused by the 1064 nm heating laser. Furthermore, the absorption maximum of the DiOC<sub>18:2</sub> fluorophore (488 nm) in the current assay is below the two-photon absorption wavelength of the 1064 nm heating laser. This, together with the high mobility of the unsaturated alkyl tails in the bilayer, results in only minor photobleaching.

As shown in Figure 2A,B, a typical melting fingerprint around a rod and sphere, respectively, consists of a circular micrometer-sized bright region centered at the metallic nanoparticle. The bright region is surrounded by a ring-shaped darker region from which the fluorophores have been depleted after partitioning into the central fluid region. To accurately determine the size of the melted fingerprint, we performed a rotational average and smoothening of the circularly symmetric melted fingerprint to obtain a radial intensity profile. The radial intensity profiles for a nanorod and a nanosphere are shown in Figure 2C,D, respectively. We defined the radius of the melted region,  $r$ , as the distance from the center of the melted region (the center of the particle) to the point where the intensity curve is equal to the background plus the noise level (before smoothening). Consistent with the results in ref 18, a control where the laser irradiated the bilayer without any particle present did not produce a detectable fingerprint.

To quantify the temperature increase,  $\Delta T$ , at a distance  $r$  from the center of a particle, one can model the nanoparticles as spherical heat radiators with an effective radius,  $R_{\text{eff}}$  placed in an infinite medium with thermal conductivity,  $\kappa$ <sup>30</sup>

$$\Delta T(r) = \frac{IC_{\text{abs}}}{4\pi r\kappa} \quad r \gg R_{\text{eff}} \quad (1)$$

Here,  $I$  is the laser intensity incident on the particle and  $C_{\text{abs}}$  is the absorption cross section of the particle at the irradiating laser wavelength. Although eq 1 was originally derived for a spherical particle of radius  $R_{\text{eff}}$  it has been proven valid for arbitrarily shaped particles at distances  $r \gg R_{\text{eff}}$  if  $R_{\text{eff}}$  is chosen as the radius of a sphere with the same volume as the particle.<sup>31</sup>

In the present case, however, the particles are not placed in an infinite medium, but on the interface between a glass coverslip and an aqueous medium. Therefore,  $\kappa$  should be replaced by  $\kappa_{\text{eff}} = \kappa/b$ , where  $b$  is a correction factor taking into account the presence of the interface.<sup>32</sup>  $b$  is determined as

$$b(r) = 1 + \frac{\kappa_1 - \kappa}{\kappa_1 + \kappa} \frac{r}{\sqrt{r^2 + 4R_{\text{eff}}^2}} \quad (2)$$

where  $\kappa$  is the thermal conductivity of water ( $0.58 \text{ W m}^{-1} \text{ K}^{-1}$ ) and  $\kappa_1$  is the thermal conductivity of glass ( $1.05 \text{ W m}^{-1} \text{ K}^{-1}$ ). The value of  $b$  as function of  $r$  for a nanosphere with radius = 100 nm and for a nanorod of dimensions  $100 \text{ nm} \times 20 \text{ nm}$  is shown in Supporting Information Figure S4.

For a constant laser intensity,  $I$ , eq 1 can be rewritten as

$$\Delta T(r) = \frac{b(r)C}{r} \quad (3)$$

where  $C = IC_{\text{abs}}/4\pi\kappa$  is a constant including all physical parameters that are difficult to determine experimentally. Using eq 3 together with knowledge of the phase transition temperature ( $T_m$ ), of the radius of the melted region,  $r_m$ , and of  $b(r_m)$  provides  $C$ . Hence, we can quantify the entire temperature profile at a given laser intensity.

As one moves closer to a nanorod, the nonspherical shape becomes important for its temperature profile. The temperature at the surface of a metallic nanorod can be calculated by introducing a morphology dependent thermal-capacitance coefficient,  $\beta$ .<sup>31</sup> Basically, the temperature at the surface can be found by dividing eqs 1 or 3 by  $\beta$  and substituting  $r$  with  $R_{\text{eff}}$ . For a sphere  $\beta = 1$  and for a nanorod  $\beta$  is a function of its aspect ratio. For a  $20 \text{ nm} \times 100 \text{ nm}$  nanorod,  $\beta$  equals to 1.16.<sup>31</sup>

The size of the melted fingerprints and the corresponding temperature profiles around irradiated nanoparticles were determined, see examples for a rod and a sphere in insets of Figure 2C,D. The orientation of the rod was parallel to the polarization vector of the laser light. Under identical illumination conditions (irradiated by  $1.8 \times 10^{10} \text{ W/m}^2$  using a 1064 nm laser), the gold nanorod ( $20 \text{ nm} \times 100 \text{ nm}$ ) and the gold nanosphere (radius  $r = 100 \text{ nm}$ ) had melting fingerprints of 1.06 and  $1.29 \mu\text{m}$  in radius, respectively. The temperature increase  $\Delta T$  at the surface of the nanorod was  $269 \text{ }^\circ\text{C}$  while the temperature increase at the surface of the spherical particle was only  $68 \text{ }^\circ\text{C}$  despite the fact that the volume of the sphere was  $\sim 100$  times that of the rod. The absorption of a nanoparticle is a function of its aspect ratio (as visualized in Supporting Information Figure S5). The rods have a broad longitudinal extinction spectrum peaking at 1000 nm (Supporting Information Figure S1B) while the 200 nm Au spheres have an extinction spectrum peaking around 527 nm in an aqueous solution. The difference in absorption between the two types of particles is caused by the fact that the NIR laser is off-resonance for the sphere but within the broad resonance peak of the rod.

Darker depletion regions surrounding the brighter fluid regions are visible in Figure 2A,B (most clearly in panel B). This decrease in intensity is caused by diffusion of fluorophores into the fluid phase from the nearby surrounding bilayer. Fluorophores more easily diffuse from the region where the temperature is within the  $1\text{--}2 \text{ }^\circ\text{C}$  interval of the phase transition (see width of heat capacity curve in Supporting Information Figure S3) than from the solid gel phase further away from the nanorod where there is a negligible diffusion at the time scale of the experiments. As the temperature gradient around the sphere is steeper at  $T_m$  than for the rod, the depletion region surrounding the sphere is less smeared out and hence easier to detect. Another visible feature is the absence of fluorophore emission at the center of the melted fingerprint. This happened instantaneously with rods (as shown in Figure 2A) and was caused by a local ablation of the lipid bilayer. For the spheres, the fluorophores in the melted fingerprint initially appeared brighter in the center possibly due

to fluorescence enhancement near the metal surface. However, after prolonged irradiation, fluorophores at the center of the fingerprint near the 200 nm gold nanoparticles also appeared darker due to local ablation of the lipid bilayer.

Contrary to the absorption spectrum of nanospheres that shows only one peak in the optical range, the plasmon resonance of gold nanorods splits into two modes, a longitudinal mode parallel to its long axis and a transverse mode orthogonal to its long axis. In our experiments, the nanorods were chosen such that their broad longitudinal resonance included the irradiating laser wavelength (Supporting Information Figure S1B shows the nanorod absorption spectrum). As the size distribution of the nanorods was relatively broad, we expected the peak of the absorption of individual rods to deviate somewhat from the peak of the ensemble graph. Figure 3A shows a series of confocal images

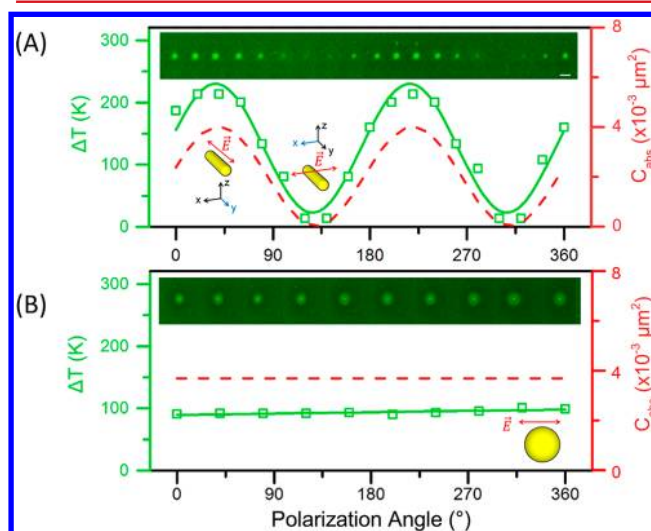


**Figure 3.** Strong dependence of gold nanorod heating on its orientation with respect to the laser polarization vector. (A) Confocal images of the melted region around a gold nanorod ( $20 \text{ nm} \times 100 \text{ nm}$ ) and corresponding surface temperature elevations as function of the rotation angle of the polarization vector (green squares). (B) Same as (A) but for a  $d = 200 \text{ nm}$  gold sphere. The scale bar of the confocal images in (A) and (B) is  $2 \mu\text{m}$ . Right axis and dashed red line in (A): DDA Simulations of the absorption cross section as function of the angle between the polarization vector and the long axis of the nanorod. Right axis and dashed red line in (B): absorption cross section for a nanosphere with  $d = 200 \text{ nm}$ .

from an experiment where a nanorod was irradiated with varying orientations of the polarization vector of the NIR laser (see also Supporting Information Video 1). The corresponding graph (left axis, green squares) shows the temperature at the surface of the gold nanorod as function of the angle of rotation of the laser polarization. The temperature increase exhibits a minimum when the rod is orthogonal to the polarization vector and a maximum when the rod is parallel to the polarization vector. Thus, we demonstrated a strong orientation dependence of the heating around an irradiated nanorod with temperature increases ranging between a few degrees Celsius and  $\sim 200 \text{ }^\circ\text{C}$  depending on the orientation of the rod. Though to our knowledge these results are the first measurements of the temperature profile around a single irradiated nanorod and of how the temperature profile depends on the orientation of the nanoparticle, our results qualitatively parallel the polar-

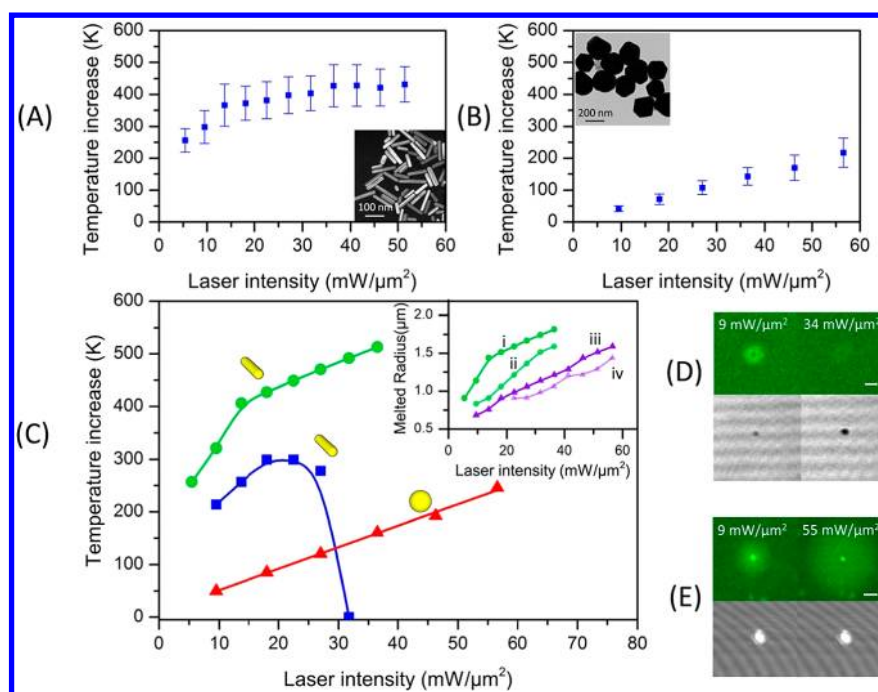


**Figure 4.** Heat-induced shape changes of irradiated nanoparticles. (A) Average surface temperature increase versus laser intensity for gold nanorods (20 nm  $\times$  100 nm,  $n = 53$ ). Inset shows TEM images of the rods. (B) As (A) but with spherical gold nanoparticles ( $d = 200$  nm,  $n = 15$ ), inset shows TEM image. (C) Heating curves versus laser intensity for two representative individual rods (green circles and blue squares, respectively) and one  $d = 200$  nm sphere (red triangles). The inset shows the radius of the melted region as a function of laser intensity for two consecutive heating cycles of two individual rods. (D,E) Fluorescent images (upper panels) and confocal reflection images (lower panels) acquired simultaneously of a gold nanorod (D) and a gold nanosphere (E) in a bilayer at two different laser intensities (left, 9 mW/ $\mu\text{m}^2$ ; right, 34 mW/ $\mu\text{m}^2$  for the gold nanorod and 55 mW/ $\mu\text{m}^2$  for the gold nanosphere). The scale bar is 1  $\mu\text{m}$ .

ization orientation dependent absorption of CdSe quantum dots<sup>33</sup> and the photothermal dependence on polarization angle of nanorods.<sup>10</sup> An identical experiment for a spherical gold nanoparticle having diameter 200 nm is shown in Figure 3B. The heating of the spherical gold nanoparticle is independent of the rotation of laser polarization.

The temperature increase is directly proportional to the absorption cross section of the nanoparticle (eq 1). The absorption cross section of a metallic nanosphere can be correctly calculated using Mie theory.<sup>34,35</sup> However, Mie theory cannot directly be used to calculate the absorption cross section of a rod. Instead, we calculated the absorption cross section of a gold nanorod by using the discrete dipole approximation (DDA).<sup>25</sup> The approximation made in the DDA is that the particle can be discretized into an array of  $N$  finite subvolumes, each constituting one polarized point dipole. These point dipoles, whose electromagnetic properties can be calculated by solving Maxwell's equations, acquire dipole moments in response to the local electric field and interact with each other. We used the DDA implementation reported in refs 36 and 37 to simulate the absorption cross section of gold nanorods (20 nm  $\times$  100 nm) for different orientations of the gold nanorod with respect to the polarization of the laser light. The calculation showed that upon radiation by 1064 nm laser, the absorption cross section of the near-resonant nanorod along its long axis ( $4.04 \times 10^{-3} \mu\text{m}^2$ ) was slightly larger than the absorption cross section ( $3.69 \times 10^{-3} \mu\text{m}^2$ ) of the off-resonant nanosphere with a 100 $\times$  larger volume. The angular dependence of the nanorod absorption cross section is shown in Figure 3A (right axis, red dashed line). The plot confirms the expected cosine square dependence of the surface temperature on the orientation of the laser polarization.<sup>10</sup>

For both nanorods and nanospheres, the size of the melted region increased with laser intensity within a certain intensity interval. At very high laser intensities, extreme temperatures were reached. The spheres could occasionally blast off the surface or explosive boiling of the water phase could occur, consistent with previous findings.<sup>18,38</sup> To avoid such extreme events, the data analyzed in the present paper were all acquired using laser intensities below  $6 \times 10^{10}$  W/ $\text{m}^2$ . However, even at low laser intensities the nanorods would be exposed to a significant heating if aligned with the laser polarization (see Figure 4A). The relatively large spread in size and shape give rise to different locations of the longitudinal resonance peak. The error bars in Figure 4A represent the corresponding heterogeneous heating ( $n = 53$ ). It should be noted that we only sampled fingerprints from irradiated nanorods which were large enough to be visible and quantified. This eliminated data from off-resonance rods whose possible fingerprints were below the diffraction limit. The temperatures of nanospheres were linearly proportional to laser intensity as expected (Figure 4B).<sup>18</sup> In contrast, the temperature increase of gold nanorods did not appear linear and leveled off at laser powers exceeding around 20 mW/ $\mu\text{m}^2$  (Figure 4A). Also, the temperature versus laser intensity relation was rather different among the individual rods probed. This heterogeneous behavior is shown for two representative rods in Figure 4C. The temperature of Rod 1 (blue squares) starts with an almost linear increase with laser intensity, subsequently the temperature begins to decrease with laser intensity, and eventually the radius of the melted region becomes too small to allow for a quantification of the temperature increase. The temperature increase of Rod 2 (green circles) initially rises rapidly and then turns over to a slower, almost linear increase. Supporting Information Figure

S6 shows additional 15 randomly chosen temperature versus intensity relations. For comparison, we also plotted the heating for a single gold nanosphere in Figure 4C (red triangles) that heats linearly with laser power as expected.

The observed change in photonic properties of irradiated nanorods probably results from a temperature induced shape change. The thermal stability of gold nanorods is much lower than that of bulk gold<sup>39</sup> and premature melting or structural changes of gold nanorods has been proven to occur at temperatures as low as  $\sim 200$  °C under conditions of prolonged heating. Under these conditions the rod restructures into a more spherical shape<sup>16</sup> thus blue shifting the resonance peak. This is supported by the data shown in the inset of Figure 4C that shows the radius of the melted region (directly proportional to surface temperature) as function of laser intensity for two heating cycles of two gold nanorods (measured individually). First, the intensity of the laser was increased and the corresponding surface temperature measured (curves i + iii), then the laser was shut down until the fingerprint disappeared and afterward laser power was again increased (curves ii + iv). For both nanorods, the surface temperature at a given laser intensity on the initial curve is smaller than the surface temperature on the re-cycle curve. This suggests that the aspect ratio of the nanorod decreased between the initial and later measurements, probably caused by a partial melting of the rod.

Moreover, the occurrence of temperature induced shape changes of irradiated nanorods was supported by confocal and reflection images of the nanoparticles before and after the heating cycle as shown in Figure 4D,E. Reflected light from small nanoparticles depends on their size as well as on their surface plasmon frequency. Since the volume of the particle stays the same, we attribute any change in reflected light to a shift in the plasmon frequency. The reflection images of small gold nanoparticles placed on a partially reflective interface like glass/water exhibit a negative contrast.<sup>40</sup> The dark spot becomes darker with increasing particle scattering up to a critical size after which the particle appears bright.<sup>40,41</sup> The reflection images of Rod 1 (blue square in Figure 4C) at two laser intensities are shown in lower half of Figure 4D (left and right image, respectively). The appearance of the particle becomes darker. This could be due to shape induced blue shift in the surface plasmon frequency resulting in higher particle scattering at 594 nm. At the same time we observed in the corresponding confocal images of the bilayer (upper images) that the temperature of the rod was higher in the first image (low laser intensity) than in the last image (higher laser intensity), which can be explained by the same blue shift of the particle resonance away from the NIR heating laser at 1064 nm. No significant changes were observed in the reflection images for the nanosphere (see Figure 4E), for which the increase of radius of the melted region was linearly proportional to the incident laser intensity.

By performing a linear fit to the data in Figure 4B and using the area of the focal region,  $A_f$  of the laser beam ( $A_f = 2.27 \mu\text{m}^2$  was measured as described in Supporting Information) the heating rate of a 200 nm sphere was found to be 1439 K/W. This is similar to the 1650 K/W reported from the same type of particle in ref 18. The temperature increase for the nanorods in Figure 4A is nonlinear, the slope of the first three data points in Figure 4A, 5897 K/W, gives a lower bound for the initial heating rate of the rods which clearly exceeds the heating rate of the  $d = 200$  nm gold spheres in Figure 4B. The initial heating

rate of an individual nanorod was found to be significantly higher than the 900 K/W reported for a  $60 \text{ nm} \times 25 \text{ nm}$  gold nanorod.<sup>14</sup> As the optically trapped rods in ref 14 were irradiated by off-resonant light, possibly displaced from the most intense part of the laser beam, and in addition performed significant fluctuations both orientation wise and in and out of focus, the heating rate in our experiment where the rod was fixed was expected to be higher.

We have measured the temperature profile around a single gold nanorod irradiated by a 1064 nm NIR laser, whose wavelength coincides with the longitudinal plasmon resonance of the rod. The temperature profile was quantified using an assay where the nanoparticle was covered by a lipid bilayer containing fluorophores with a phase dependent partitioning. The relatively high accuracy of this method is caused by the fact that only light from the exact plane of the irradiated particle contributes to the signal. If also the polarization anisotropy of the fluorophores was detected,<sup>23</sup> the method could be expanded, for example, to measurements on natively fluid cellular membranes. The temperature profile of an irradiated gold nanorod was found to be highly dependent on its orientation with respect to the laser polarization vector. The temperature increase was highest if they were parallel and nearly vanished if orthogonal. A resonant nanorod oriented parallel to the polarization vector attained temperatures significantly higher than a nonresonant spherical gold nanoparticle having a 100 times larger volume. Hence, gold nanorods are an excellent choice as remotely controlled heat transducers in, for example, medical applications where space is limited or where delivery of nanoparticles depends critically on size and where NIR radiation is preferred. When a gold nanorod was exposed to temperature increases exceeding 200 °C, we observed a partial melting of the rod into a more spherical shape, thus changing its absorption properties significantly. The fact that gold nanorods lose their ability to efficiently transform electromagnetic radiation into heat upon excessive heating is important to consider for photothermal applications.

## ■ ASSOCIATED CONTENT

### 📄 Supporting Information

Supplementary methods as well as additional figures and video. This material is available free of charge via the Internet at <http://pubs.acs.org>.

## ■ AUTHOR INFORMATION

### Corresponding Author

\*E-mail: [oddershede@nbi.dk](mailto:oddershede@nbi.dk).

### Notes

The authors declare no competing financial interest.

## ■ ACKNOWLEDGMENTS

We thank S. N. S. Reihani for fruitful discussions, A. Kyrsting for assistance with measuring the radius of the focal region, I. Jensen for assistance with the electron microscopy, and S. B. Madsen for assistance with the calorimetric measurements. This research was financially supported by a Niels Bohr Scholarship, the Carlsberg foundation, and a University of Copenhagen Excellence grant.

## ■ REFERENCES

- (1) Liu, H.; Chen, D.; Tang, F.; Du, G.; Li, L.; Meng, X.; Liang, W.; Zhang, Y.; Teng, X.; Li, Y. Photothermal Therapy of Lewis Lung Carcinoma in Mice using Gold Nanoshells on Carboxylated Polystyrene Spheres. *Nanotechnology* **2008**, *19*, 455101.
- (2) Lal, S.; Clare, S. E.; Halas, N. J. Nanoshell-Enabled Photothermal Cancer Therapy: Impending Clinical Impact. *Acc. Chem. Res.* **2008**, *41*, 1842–1851.
- (3) Boyer, D.; Tamarat, P.; Maali, A.; Lounis, B.; Orrit, M. Photothermal Imaging of Nanometer-Sized Metal Particles Among Scatterers. *Science* **2002**, *297*, 1160–1163.
- (4) Tong, L.; Wei, Q.; Wei, A.; Cheng, J. Gold Nanorods as Contrast Agents for Biological Imaging: Optical Properties, Surface Conjugation and Photothermal Effects. *Photochem. Photobiol.* **2009**, *85*, 21–32.
- (5) Bardhan, R.; Grady, N. K.; Cole, J. R.; Joshi, A.; Halas, N. J. Fluorescence Enhancement by Au Nanostructures: Nanoshells and Nanorods. *ACS Nano* **2009**, *3*, 744–752.
- (6) Kawano, T.; Niidome, Y.; Mori, T.; Katayama, Y.; Niidome, T. PNIPAM Gel-Coated Gold Nanorods for Targeted Delivery Responding to a Near-Infrared Laser. *Bioconjugate Chem.* **2009**, *20*, 209–212.
- (7) Huang, X.; El-Sayed, I. H.; Qian, W.; El-Sayed, M. A. Cancer Cell Imaging and Photothermal Therapy in the Near-Infrared Region by Using Gold Nanorods. *J. Am. Chem. Soc.* **2006**, *128*, 2115–2120.
- (8) Muskens, O. L.; Gianini, V.; Sánchez-Gil, J. A.; Gómez Rivas, J. Optical Scattering Resonances of Single and Coupled Dimer Plasmonic Nanoantennas. *Opt. Express* **2007**, *15*, 17736–17746.
- (9) Baffou, G.; Quidant, R.; Girard, C. Heat Generation in Plasmonic Nanostructures: Influence of morphology. *Appl. Phys. Lett.* **2009**, *94*, 153109.
- (10) Chang, W. S.; Ha, J. W.; Slaughter, L. S.; Link, S. Plasmonic Nanorod Absorbers as Orientation Sensors. *Proc. Natl. Acad. Sci. U.S.A.* **2010**, *107*, 2781–2786.
- (11) Svoboda, K.; Block, S. M. Optical Trapping of metallic Rayleigh Particles. *Opt. Lett.* **1994**, *19*, 930–932.
- (12) Hansen, P. M.; Bhatia, V. K.; Harrit, N.; Oddershede, L. Expanding the Optical Trapping Range of Gold Nanoparticles. *Nano Lett.* **2005**, *5*, 1937–1942.
- (13) Selhuber-Unkel, C.; Zins, I.; Schubert, O.; Sönnichsen, C.; Oddershede, L. B. Quantitative Optical Trapping of Single Gold Nanorods. *Nano Lett.* **2008**, *8*, 2998–3003.
- (14) Ruijgrok, P. V.; Verhart, N. R.; Zijlstra, P.; Tchegbotareva, A. L.; Orrit, M. Brownian Fluctuations and Heating of an Optically Aligned Gold Nanorod. *Phys. Rev. Lett.* **2011**, *107*, 037401.
- (15) Horiguchi, Y.; Honda, K.; Kato, Y.; Nakashima, N.; Niidome, Y. Photothermal Reshaping of Gold Nanorods Depends on the Passivating Layers of the Nanorod Surfaces. *Langmuir* **2008**, *24*, 12026–12031.
- (16) Petrova, H.; Juste, J. P.; Pastoriza-Santos, I.; Hartland, G. V.; Liz-Marzán, L. M.; Mulvaney, P. On the Temperature Stability of Gold Nanorods: Comparison between Thermal and Ultrafast Laser-Induced Heating. *Phys. Chem. Chem. Phys.* **2006**, *8*, 814–821.
- (17) Ungureanu, C.; Kroes, R.; Petersen, W.; Groothuis, T. A. M.; Ungureanu, F.; Janssen, H.; Leeuwen, F. W. B.; Kooyman, R. P. H.; Manohar, S.; Leeuwen, T. G. Light Interactions with Gold Nanorods and Cells: Implications for Photothermal Nanotherapeutics. *Nano Lett.* **2011**, *11*, 1887–1894.
- (18) Bendix, M. P.; Reihani, S. N. S.; Oddershede, L. B. Direct Measurements of Heating by Electromagnetically Trapped Gold Nanoparticles on Supported Lipid Bilayers. *ACS Nano* **2010**, *4*, 2256–2262.
- (19) Kyrsting, A.; Bendix, P. M.; Stamou, D. G.; Oddershede, L. B. Heat Profiling of Three-Dimensionally Optically Trapped Gold Nanoparticles using Vesicle Cargo Release. *Nano Lett.* **2011**, *11*, 888–892.
- (20) Urban, A. S.; Fedoruk, M.; Horton, M. R.; Rädler, J. O.; Stefani, F. D.; Feldmann, J. Controlled Nanometric Phase Transitions of Phospholipid Membranes by Plasmonic Heating of Single Gold Nanoparticles. *Nano Lett.* **2009**, *9*, 2903–2908.
- (21) Carlson, M. T.; Khan, A.; Richardson, H. H. Local Temperature Determination of Optically Excited Nanoparticles and Nanodots. *Nano Lett.* **2011**, *11*, 1061–1069.
- (22) Seol, Y.; Carpenter, A. E.; Perkins, T. T. Gold nanoparticles: enhanced optical trapping and sensitivity coupled with significant heating. *Opt. Lett.* **2006**, 2429–2431.
- (23) Baffou, G.; Kreuzer, M. P.; Kulzer, F.; Quidant, R. Temperature Mapping near Plasmonic Nanostructures using Fluorescence Polarization Anisotropy. *Opt. Express* **2009**, *17*, 3291–3298.
- (24) Baffou, G.; Bon, P.; Savatier, J.; Polleux, J.; Zhu, M.; Merlin, M.; Rigneault, H.; Monneret, S. Thermal Imaging of Nanostructures by Quantitative Optical Phase Analysis. *ACS Nano* **2012**, *6* (3), 2452–2458.
- (25) Purcell, E. M.; Pennypacker, C. R. Scattering and Absorption of Light by Nonspherical Dielectric Grains. *Astrophys. J.* **1973**, *186*, 705–714.
- (26) Richardson, A. C.; Reihani, N.; Oddershede, L. B. Combining Confocal Microscopy with Precise Force-Measuring Optical Tweezers. *Proc. SPIE* **2006**, 6326, 28–38.
- (27) Baumgart, T.; Hunt, G.; Farkas, E. R.; Webb, W. W.; Feigenson, G. W. Fluorescence Probe Partitioning between Lo/Ld Phases in Lipid Membranes. *Biochim. Biophys. Acta* **2007**, *1768*, 2182–2194.
- (28) Seu, K. J.; Pandey, A. P.; Haque, F.; Proctor, E. A.; Ribbe, A. E.; Hovis, J. S. Effect of Surface Treatment on Diffusion and Domain Formation in Supported Lipid Bilayers. *Biophys. J.* **2008**, *92*, 2445–2450.
- (29) Seeger, H. M.; Di Cerbo, A.; Alessandrini, A.; Facci, P. Supported Lipid Bilayers on Mica and Silicon Oxide: Comparison of the Main Phase Transition Behavior. *J. Phys. Chem. B* **2010**, *114*, 8926–8933.
- (30) Goldenberg, H.; Tranter, C. J. Heat Flow in an Infinite Medium Heated by a Sphere. *Br. J. Appl. Phys.* **1952**, *3*, 296–298.
- (31) Baffou, G.; Quidant, R.; García de Abajo, F. J. Nanoscale control of optical heating in complex plasmonic systems. *ACS Nano* **2010**, *4*, 709–716.
- (32) Baffou, G.; Quidant, R.; Girard, C. Thermoplasmonics modelling: A green function approach. *Phys. Rev. B* **2010**, *82*, 165424.
- (33) Empedocles, S. A.; R. Neuhauser, R.; Bawendi, M. G. Three-dimensional orientation measurements of symmetric single chromophores using polarization microscopy. *Nature* **1999**, *399*, 126–130.
- (34) Mie, G. Beiträge zur Optik Trüber Medien, Speziell Kolloidaler Metallösungen. Leipzig. *Ann. Phys.* **1908**, *25*, 377–445.
- (35) Kreibig, U.; Vollmer, M. Optical Properties of Metal Clusters. In *Springer Series in Materials Science*; Springer: Berlin, 1995.
- (36) Yurkin, M. A.; de Kanter, D.; Hoekstra, A. G. Accuracy of the Discrete Dipole Approximation for Simulation of Optical Properties of Gold Nanoparticles. *J. Nanophotonics* **2010**, *4*, 041585–15.
- (37) Yurkin, M. A.; Hoekstra, A. G. The Discrete-Dipole-Approximation Code ADDA: Capabilities and Known Limitations. *J. Quant. Spectrosc. Radiat. Transfer* **2011**, *112*, 2234–2247.
- (38) Kotaidis, V.; Dahmen, C.; von Plessen, G.; Springer, F.; Plech, A. Excitation of Nanoscale Vapor Bubbles at the Surface of Gold Nanoparticles in Water. *J. Chem. Phys.* **2006**, *124*, 184702.
- (39) Tollan, C. M.; Marcilla, R.; Pomposo, J. A.; Rodriguez, J.; Aizpurua, J.; Molina, J.; Mecerreyes, D. Irreversible Thermochromic Behavior in Gold and Silver Nanorod/Polymeric Ionic Liquid Nanocomposite Films. *ACS Appl. Mater. Interfaces* **2009**, *1*, 348–352.
- (40) Jacobsen, V.; Stoller, P.; Brunner, C.; Vogel, V.; Sandoghdar, V. Interferometric Optical Detection and Tracking of Very Small Nanoparticles at a Water-Glass Interface. *Opt. Express* **2006**, *14*, 405–414.
- (41) Bosanac, L.; Aabo, T.; Bendix, P. M.; Oddershede, L. B. Efficient Optical Trapping and Visualization of Silver Nanoparticles. *Nano Lett.* **2008**, *8*, 1486–1491.